Increased material differentiation through multi-contrast x-ray imaging: a preliminary evaluation of potential applications to the detection of threat materials

To cite this article before publication: Alberto Astolfo *et al* 2023 *Phys. Scr.* in press https://doi.org/10.1088/1402-4896/ace939

Increased material differentiation through multi-contrast x-ray imaging: a preliminary evaluation of potential applications to the detection of threat materials

A. Astolfo[1,2], I.G. Haig[2], D. Bate[2,1], A. Olivo[1,*], P. Modregger[3,4]

1. Department of Medical Physics and Biomedical Engineering, UCL, London WC1E 6BT, UK
2. Nikon X-Tek Systems Ltd, Tring, Herts, HP23 4JX, UK
3. Department of Physics, University of Siegen, 57072 Siegen, Germany
4. Center for X-ray and Nano Science CXNS, Deutsches Elektronen-Synchrotron DESY, 22607 Hamburg, Germany

* Corresponding author, Email: a.olivo@ucl.ac.uk

Abstract

Most material discrimination in security inspections is based on dual-energy x-ray imaging, which enables the determination of a material's effective atomic number (Z_{eff}) as well as electron density and its consequent classification as organic or inorganic. Recently phase-based "dark-field" x-ray imaging approaches have emerged that are sensitive to complementary features of a material, namely its unresolved microstructure. It can therefore be speculated that their inclusion in the security-based imaging could enhance material discrimination, for example of materials with similar electron densities and Z_{eff} but different microstructures. In this paper, we present a preliminary evaluation of the advantages that such a combination could bear. Utilising an energy-resolved detector for a phase-based dark-field technique provides dual-energy attenuation and dark-field images simultaneously. In addition, since we use a method based on attenuating x-ray masks to generate the dark-field images, a fifth (attenuation) image at a much higher photon energy is obtained by exploiting the x-rays transmitted through the highly absorbing mask septa. In a first test, a threat material is imaged against a non-threat one, and we show how their discrimination based on maximising their relative contrast through linear combinations of two and five imaging channels leads to an improvement in the latter case. We then present a second example to show how the method can be extended to discrimination against more than one non-threat material, obtaining similar results. Albeit admittedly preliminary, these results indicate that significant margins of improvement in material discrimination are available by including additional x-ray contrasts in the scanning process.

Introduction

Security inspections at e.g., airports are based on dual-energy x-ray imaging methods [1,2]. Images created at two significantly different (average) x-ray energies can be processed with established algorithms [3,4] in an attempt to determine the electron density and the effective atomic number (Z_{eff}) of the scanned material. Subsequent research looked into the possibility to use more than two energies [5,6], typically demonstrating better material determination or reduced uncertainty.

As a completely independent line of research, phase-based x-ray imaging, gained momentum in the mid-90s [7-9], following pioneering developments in the mid-60s [10]. Alongside the ability to detect phase changes, access to an additional "contrast channel" was demonstrated in the early 00s [11-13], which was termed dark-field or "Ultra-Small Angle X-Ray Scatter" (USAXS) imaging. This contrast channel is related to the degree of

inhomogeneity that the imaged object presents on a scale smaller than the spatial resolution, and indeed this signal was later on connected to "traditional" small-angle x-ray scatter [14-15]. Technology was then developed that enables translating initially the phase-based methods [16,17], then also the dark-field capabilities [18-19] for use with conventional, laboratory-based x-ray sources, which made the technology more widely available.

The research presented in this paper combines all of the above through the use of a scanner based on one of the existing laboratory-based phase technologies ("edge illumination", EI), which uses apertured masks to generate phase sensitivity [17,19-21]. Thanks to the use of a detector with energy-thresholding capabilities [22], the scanner is capable of delivering five contrast channels (attenuation at three different energies and dark-field at two) through a single object scan. More specifically, the detector threshold allows splitting the used x-ray spectrum in two, resulting in the collection of high and low energy attenuation (Abs_H, Abs_L) and dark-field ($Scatt_H$, $Scatt_L$) images. In addition to this, the small percentage of x-rays transmitted through the mask septa are also collected, resulting in the creation of a fifth attenuation image at a much higher average X-ray energy. We refer to this contrast as "offset" image, as it corresponds to the intensity detected between two consecutive beamlets formed by the apertures, i.e., the offset above which the beamlet intensity is detected. The system is also capable of simultaneously registering differential phase at two energies [23,24], but this property is not exploited in this study.
Alongside the established methods that exist to combine attenuation-based images at different energies [3-6], recently approaches have emerged that address dual-energy dark field imaging in a quantitative manner [25].

This paper follows a more basic, simplified approach in which the detection of a material of interest (e.g., an explosive) is maximised against other materials by producing a linear combination of the various contrast channels with floating coefficient, and selecting the set of coefficients that results in the maximum contrast-to-noise ratio (*CNR*). This is done both on Abs_H, Abs_L only, as a surrogate for conventional dual-energy imaging, and with the full set of five contrasts (Abs_H, Abs_L, Offest, $Scatt_H$, $Scatt_L$). Despite the simplicity of the approach, the comparison of the optimised *CNR* in the two cases provides an estimate of the detection advantages that can be obtained by simultaneously exploiting five contrasts instead of two. After laying out the procedure to distinguish two materials from each other and presenting a practical example, we outline an approach that can be used to maximise the detection of a material of interest against multiple others. Although in both cases we provide examples in a security context, the proposed approach is general, and can be applied to the discrimination of any type of materials.

Materials and methods

A schematic of the imaging system is shown in Fig. 1. It features a tungsten X-Tek (Tring, UK) 160 x-ray tube with an approximately 80 micron focal spot, operated at 80 kVp and 2 mA. The detector was a CdTe CMOS-based photon counter XC-Flite FX2 manufactured by Direct Conversion. It has 100 micron square pixels and an overall field of view of 20 cm (vertical) times 1.28 cm (horizontal). The detector features two thresholds, one of which is used to cut off the noise, and the other to split the spectrum in two. This was calibrated at the

beginning of the experiment by comparing experimental measurements with a theoretical model.

The masks were fabricated to the authors' design by Creatv Microtech (Rockville, MD), by electroplating a ~200 micron thick gold layer on a patterned graphite substrate. Pre-sample and detector masks were placed at 1.50 and 1.95 m from the source, respectively, with the detector placed immediately downstream of the detector mask; their overall size matches the detector's once magnification is taken into account. Aperture sizes were 28 μm and 21.4 μm for detector and pre-sample mask, respectively.

While a symmetric mask is shown for simplicity in Fig. 1, in truth the system employs the "asymmetric" mask concept [26] that enables the acquisition of all image frames necessary for the retrieval of attenuation, differential phase and dark-field images in a single object scan. Both masks are mounted on motor stacks that enables their alignment with each other and with the detector's pixel columns; a third, longer translation stage is used to scan the objects through the beam, simulating the use of a conveyor beld in e.g. an airport scanner for carry-on baggage. Each scan point was measured for 1 s, which resulted in a total scan time of about 45 min. A thorough discussion on scan times is available in [23].

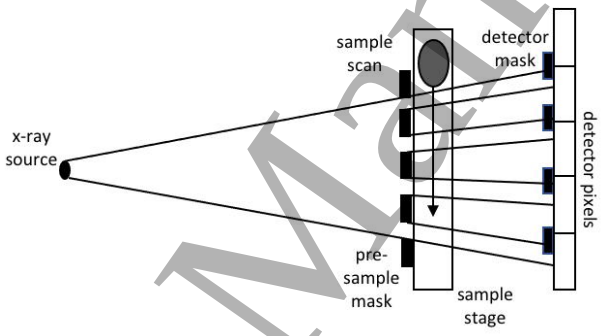

Fig 1 schematic diagram of the used imaging system

Scans with the sample present are acquired alongside "air" scans, and the intensity, central position, and full-width at half maximum (FWHM) of the beamlets are compared on a pixel-by-pixel basis. More specifically, beamlets are fitted with Gaussian curves in both cases, at which point the pixelwise ratio between curve areas provides the sample's attenuation, and the difference between curve centres and FWHMs the refraction and dark-field signals, respectively. In the latter two cases, division by the sample-to-detector distance enables converting beamlet shifts/broadenings on the detector into angular values; a full equation-based description is not repeated here for simplicity's sake, and the reader is referred to recent publications [23,27].

Two phantoms simulating explosive concealment in a postal delivery were created to demonstrate the technology in a security-related application. The first one, aimed at developing and testing the approach, was deliberately simpler. It consisted of a thin (2 cm) plastic box with a size of 4 cm by 4 cm containing Semtex H1 placed alongside a stack of post-its with comparable thickness inside a standard paper envelope. In the second phantom, the same plastic box containing a different explosive (TNT) was placed alongside other objects inside a thicker cardboard box. In particular, a highlighter pen and a makeup

removal pad were placed near the explosive, to develop a procedure that allows to simultaneously discriminate the explosive from more than one surrounding material. For both phantoms non-threat materials with a pronounced microstructure were chosen in order to 1) provide an appreciable dark-field signal and, thus, 2) to provide a challenge for discrimination of threat vs. non-threat materials.

As the quantitative parameter to determine the degree of material discrimination, we used the *CNR*, defined as:

$$CNR = \frac{|mean(ROI_1) - mean(ROI_2)|}{\sqrt{stdv(ROI_1)^2 + stdv(ROI_2)^2}} \quad (1)$$

$ROI_{1,2}$ indicate Regions-Of-Interest selected inside the threat and non-threat material, respectively. The module at the numerator guarantees that the *CNR* is a positive value, and *stdv* indicates the standard deviation. The availability of five different contrast channels means that for a given set of 2 materials five different *CNR*s are available. We introduce the linear combination of individual contrast channels in order to provide an integration of all contrasts into a single image:

$$I = a_1 I_{\mathrm{Abs}_L} + a_2 I_{\mathrm{Abs}_H} + a_3 I_{\mathrm{Offset}} + a_4 I_{\mathrm{Scatt}_L} + a_5 I_{\mathrm{Scatt}_H}, \quad (2)$$

where $a_{1\text{-}5}$ are free coefficients, and the pedices Abs_L, Abs_L, *Offset*, $Scatt_L$, $Scatt_H$ refer to the intensities detected in the corresponding images. The *CNR* between two materials is then calculated while iterating over $a_{1\text{-}5}$ for the 5-contrast case, and over $a_{1\text{-}2}$ only for the dual energy "surrogate", and the set of coefficients resulting in the highest *CNR* value is selected. When only two materials need to be discriminated (first phantom), the above procedure is straightforward. When a certain target material (in our case the explosive) needs to be discriminated against more than one material (e.g. two, as in our second phantom), a two-step process is required. First, we calculated the minimum CNR between the material pairs for given set of coefficients $a_{1\text{-}5}$, which aims at the discrimination of threat materials from *all* non-threat materials. Second, we then iterate over coefficients $a_{1\text{-}5}$, and choose the set of coefficients that maximises the minimum CNR. This simultaneously maximises the distance (in *CNR* terms) between all three materials, which accounts for the possibility that the *ROI* corresponding to the material of interest is not known *a priori*.

Results and Discussion

The utilized detector allows for the simultaneous acquisition of a low and a high photon energy image by setting a threshold voltage, which corresponds to a specific photon energy threshold, the value of which is unknown prior to calibration. Thus, the initial step was the calibration of the detector's higher threshold (Fig 2), which is described in the following.

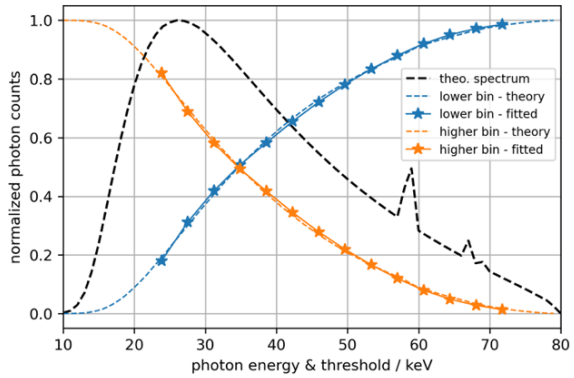

Fig 2 calibration of the higher detector threshold

We started from the theoretical (normalised) 80 kVp spectrum of a tungsten source, obtained through SpekCalc [28-30] and represented by the dashed black line in Fig. 2. The dashed orange and blue lines show the fraction of number of photons in the higher and lower energy bins (respectively) as a function of the threshold in keV $f_{theo,h}(E_{th})$ and $f_{theo,l}(E_{th})$ (with $f_{theo,h}(E_{th}) + f_{theo,l}(E_{th}) = 1$), calculated from the same theoretical spectrum. In the experiment, we scanned the voltage threshold in steps of 1 V and extracted the fraction of number of photons in the corresponding energy bins yielding $f_{\exp,h}(V_{th})$ and $f_{\exp,l}(V_{th})$. We assumed a linear transformation between the photon energy and the voltage threshold, i.e., $E_{th} = mU_{th} + b$. In order to retrieve the calibration parameters m and b we numerically solved the minimisation problem

$$\min_{m,\,b} \sum_i (f_{theo,h}(E_{th,i}) - f_{\exp,h}(mU_{th,i} + b))^2, \tag{3}$$

where *i* denotes the individual scan points. The result of this calibration was $E_{th}[keV] = 3.69[keV]/[V] * U_{th}[V] + 7.2[keV]$ with E_{th} the energy threshold in keV and U_{th} the threshold value in V. The solid orange and blue lines with markers in Fig. 2 show the experimental fraction of counts for the high and low energy bins as transformed by the calibration procedure. As can be seen the curves match very well with their theoretical counterparts, which validates the described calibration procedure.
The second preliminary step consisted in an outline determination of the threshold value that leads to an optimal material discrimination. In principle, this requires the prior knowledge of the specific contrast values produced by the various materials in the different imaging channels. However, some degree of optimisation can be conducted on the basis of the background noise minimisation as previously reported in [31].

The first step in this process is the determination of the system's sensitivity function, which in EI is the *illumination curve* (IC), obtained by scanning the pre-sample mask in the absence of a sample while the remainder of the imaging system is kept stationary [32]. This is modelled as a convolution between the (re-scaled) source distribution and the apertures in the pre-sample and detector masks, while taking into account a degree of transmission through the masks that gives rise to the IC's offset (Fig. 3a):

$$\mathrm{IC}(m) = (1 - t)S(m) \otimes A_1(m) \otimes A_2(m) + t \tag{4}$$

with m , the sample mask position, $S(m)$, the Gaussian-shaped source distribution, $A_1(m)$and $A_2(m)$, the apertures of the sample and detector mask, respectively, the aperture of the detector mask and t, the transmission through the mask for the given energy threshold and $\otimes$the convolution operator. An example of the resulting IC is displayed in Fig. 3a as the blue curve.

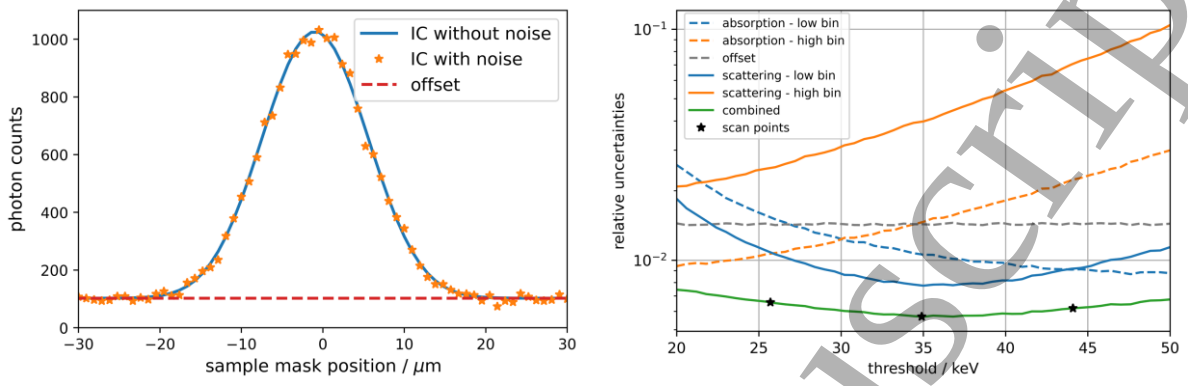

(a) (b)

Fig 3 modelling of the system's illumination curve (a) and noise behaviour in the various retrieved contrast channels as a function of the detector threshold (b). The green curve in (b) represents the combination of noise in each contrast channel via inverse-variance weighting (eq. 6), and the black stars show the threshold values at which experimental images were collected in this study.

Then photon shot noise was added to the modelled ICs (orange markers in Fig. 3a) and the curve's integral signal (representative of absorption) and the signal width (corresponding to scattering) were determined by moment analysis [33]. This was repeated 10,000 times and the resulting relative uncertainties over the repetitions were calculated (Fig. 3b). Please note that this model only reflects the noise behaviour of reference scans (i.e., without sample) and not directly that of attenuation or scattering contrasts.

In order to coarsely model the potential gain in material discrimination by combining the different contrast channels (eq. 2), we have used inverse-variance weighting of the relative uncertainties, which is known to minimize the variance of the weighted average [34]. For the linear combination of different contrasts this leads to

$$I = \frac{\sum_j I_j / {u_j}^2}{\sum_j 1 / {u_j}^2} \tag{5}$$

with I_j, the *i*th contrast channel (ref eq. 2) and u_j, the corresponding relative uncertainty. Naturally, the contrast values $I_j$depend on the materials in question. But the uncertainty of the weighted average composite contrast $I$is independent from the specific I_j:

$$u_I = \frac{1}{\sqrt{\sum_j 1 / {u_j}^2}}. \tag{6}$$

Fig. 3(b) shows the relative uncertainties in the various contrast channels as a function of the energy threshold in keV. Their combination as an inverse-variance weighted sum (green curve) provides an indication of the threshold value for which the combined relative uncertainty u_I arising from all contrast values is minimised. As can be seen, the process is dominated by $Scatt_L$, and presents a broad minimum around 35 keV.

While developing this process we observed that, despite the nominal gold thickness in the masks being 200 μm, a better match with the experimentally observed offset value is obtained with a gold thickness of 150 μm. This is not unprecedented, as masks are often affected by some degree of underplating as well as a reduced density compared to solid gold's nominal value [35]. However, this can be difficult to determine precisely as other factors (source tails, air scattering) can affect the offset value. For this reason, the above process was repeated using a gold thickness of 200 μm, with the results reported in the supplementary materials (suppl. fig. 1). As can be seen from that figure, the overall trend is very similar, with possibly a slight shift of the "optimal" threshold towards higher values. However, the broadness of the maximum and the indicative nature of the exercise (since, as mentioned, real contrasts are unknown *a priori*) means very similar indications are obtained in the two cases. However, to take this into account, the following *CNR* optimisation processes were repeated at three different threshold values, indicated with black stars in Fig. 3(b).

Fig. 4 presents the five retrieved images for the simpler, "two-material" phantom acquired with a detector threshold of 35 keV, which roughly matches the expected optimal noise behaviour as observed in Fig. 3(b). Paper (post-its) and Semtex 1H are visible on the left and right-hand sides, respectively. The blocky structures visible in the bottom of the images are the sample holders while the paper envelope holding the post-its and the Semtex sample is not visible. The scalebar in Fig. 4(a) is 4 cm. The ROIs from which mean and stdv values have been extracted for CNR calculation are shown in Fig. 4(a), with blue and red corresponding to paper and Semtex, respectively. The contrast against the background ("BG", black ROI) has also been calculated for completeness, although it has not been used for further calculations. The CNR in each image for each pair of materials is reported in the table at the bottom right corner. The second column in the table at the bottom right corner provides the "natural" contrast between post-its and Semtex in the various contrast channels. For completeness, the same table reports also the *CNR* of the two materials against the background (the envelope), although this has not been used in further analysis.

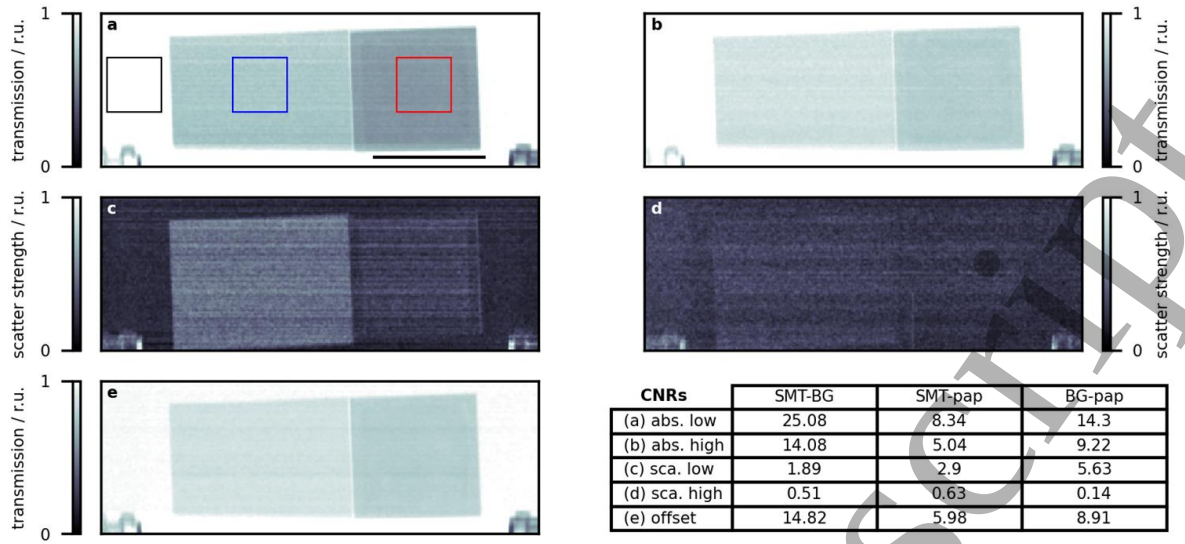

CNRs	SMT-BG	SMT-pap	BG-pap
(a) abs. low	25.08	8.34	14.3
(b) abs. high	14.08	5.04	9.22
(c) sca. low	1.89	2.9	5.63
(d) sca. high	0.51	0.63	0.14
(e) offset	14.82	5.98	8.91

Fig 4 retrieved Abs_L (a), Abs_H (b), $Scatt_L$ (c) $Scatt_H$ (d) and Offset (e) images for the "two materials" phantom acquired with a detector threshold of 35 keV. The table on the bottom right hand side lists CNRs of interest.

Fig 5 reports the result of the "optimised linear contrast combination" applied to the above dataset, for two (top row) and five (bottom row) contrasts. Here, we have searched the parameter space (i.e.,$a_1$and $a_2$in the case of the dual-energy surrogate contrast anda_1-$a_5$in the case of the combination of the 5 contrasts; see eq. (2)) for the set of parameters that maximise the *CNR* between Semtex and paper. As the *CNR* is independent from constant factors this effectively reduces the parameter space to one independent variable in the dual-energy case, and to four independent variables in the 5 contrast case. The searches were performed numerically as a minimisation of the negative *CNR* by gradient descent:

$$\min_{a_i} -CNR_{SEMTEXvPAPER}(a_i) \tag{7}$$

with $a_i$denoting the appropriate set of parameters. Individual contrast channels were binned four times to emulate larger pixel sizes (effective pixel size ≈ 400 µm) and subsequently normalised to have zero mean and a standard deviation of one prior to *CNR* optimisation. The ROI for *CNR* determination was 50 by 50 pixels.

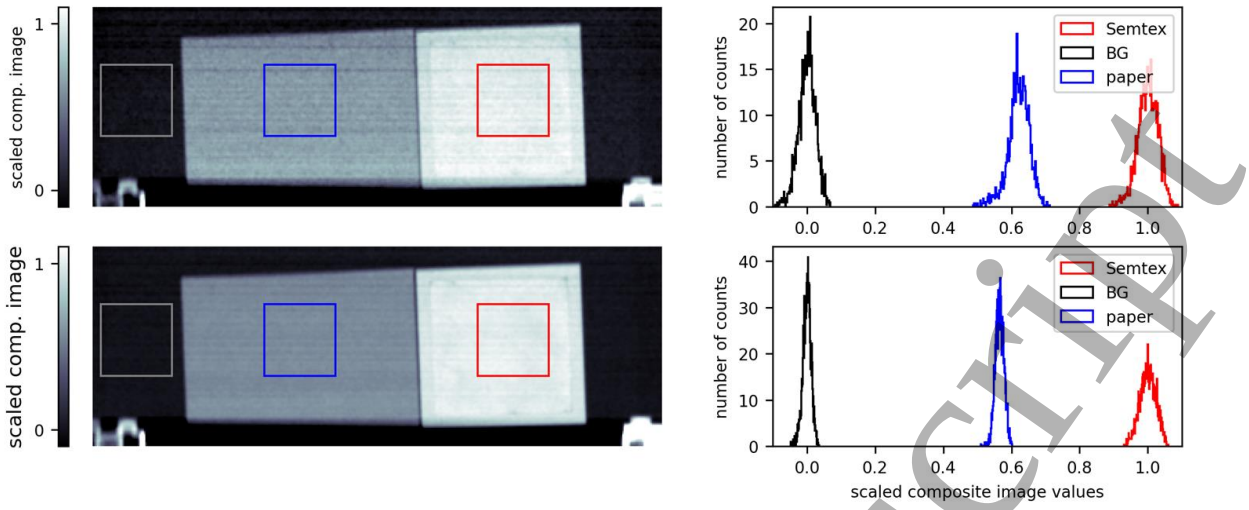

Fig 5 CNR optimisation at a 35 keV threshold for two (Abs_L and Abs_H, top row) and five (bottom row) contrasts. The re-scaled composite images are shown on the left. Corresponding histograms extracted from the selected ROIs are shown at the right-hand side of each image (BG = background, i.e., the envelope).

On the left-hand side of Fig 5 the scaled composite images are shown for dual-energy (top row) and 5 contrast combination (bottom row). In order to facilitate comparability between different phantoms and energy thresholds, the values of the composite images have been rescaled in such a way that the backround has zero mean while the threat material has a mean of one. The improvement in *CNR* is best appreciated by looking at the histograms on the right-hand side of each image, from which it is immediately evident that combining five contrasts makes the histograms much narrower and therefore the materials more neatly separated from each other. Optimised Semtex-paper (i.e., post-its) *CNR* values are 8.7 and 16.3 for the combination of two and five contrast respectively, indicating an almost 100% improvement resulting from the use of the three additional contrasts. By comparing this with the values reported in the second column at the bottom right corner of Fig 4, it can be noticed that the combination of Abs_L *and* Abs_H alone leads to a very small improvement over the attenuation values used on their own. We attribute the mere small improvement of combining the standard dual-energy contrasts to the fact that the noise between the Abs_L and Abs_H contrast channels was correlated *(r=0.42),* which can be explained by a redistribution of some photons from the high energy bin (i.e., Abs_H) to the low energy bin (i.e., Abs_L) by charge sharing [36]. Combining five contrasts, on the other hand, significantly outperforms all "native" values.

This exercise was repeated for detector thresholds of 26 and 44 keV, resulting in optimised *CNR* values of 7.7 and 9.3 (respectively) in the "two contrast" case, and of 15.1 and 15.4 in the "five contrast" case. This seems to indicate that the identification of 35 keV as the optimal threshold for the combination of five contrasts (Fig 3(b)) holds in the five-contrast case, although differences are small, as can be expected from the broadness of the minimum in the combined noise plot. The same does not apply to the two-contrast case (for which a 44 keV threshold gives a slightly higher value), however this could be expected as the combination of the noise levels was dominated by $Scatt_L$. Overall, the small differences among the above values indicates that a reasonable choice of threshold that roughly splits the spectrum in half provides close to optimal values, again in line with the broadness of the

minimum observed in Fig. 3(b). The full datasets at thresholds 26 and 44 keV and their processed versions are reported for completeness in the supplementary materials, suppl. fig. 2 to 5.

Finally, Fig. 6 shows the five retrieved images for the more complex phantom, still with a detector threshold of 35 keV. Pad, highlighter pen and TNT are visible from left to right in the images. The blocky structures visible in the bottom of the images are the sample holders. The ROIs from which mean and stdv values have been extracted for the CNR calculations are shown in Fig. 6(a), with blue, green, and red corresponding to pad, pen and TNT, respectively. The contrast between TNT and background ("BG", black ROI) has also been calculated for completeness, although it has not been used for further calculations. The CNR in each image for each pair of materials is summarised in the table at the bottom right corner.

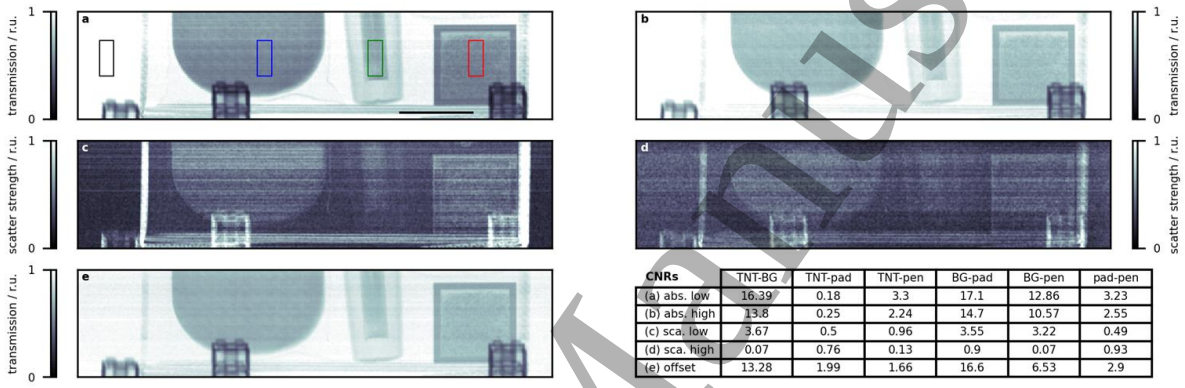

CNRs	TNT-BG	TNT-pad	TNT-pen	BG-pad	BG-pen	pad-pen
(a) abs. low	16.39	0.18	3.3	17.1	12.86	3.23
(b) abs. high	13.8	0.25	2.24	14.7	10.57	2.55
(c) sca. low	3.67	0.5	0.96	3.55	3.22	0.49
(d) sca. high	0.07	0.76	0.13	0.9	0.07	0.93
(e) offset	13.28	1.99	1.66	16.6	6.53	2.9

Fig. 6 retrieved Abs_L (a), Abs_H (b), $Scatt_L$ (c) $Scatt_H$ (d) and Offset (e) images for the "three materials" phantom acquired with a detector threshold of 35 keV. The table on the bottom right hand side lists CNRs of interest.

The columns of interest in the (more complex, due to the increased number of materials) table in the bottom right corner of Fig. 6 are the second and the third, indicating the "natural" *CNR* of TNT against pad and pen, respectively. As can be seen, in this case we are dealing with significantly lower contrasts than in the more simplistic case of two materials only, which we are aiming to enhance through the five-contrast combination process.

The corresponding results are shown in Fig. 7. For this more complex phantom, the search for the optimal parameter set in eq. (2) in terms of the *CNR* was more elaborate. For each given parameter set a_1-a_5 there are two *CNR*s are of interest: TNT vs pen and TNT vs pad. The smaller of those two *CNR*s will limit the differentiation between threat and non-threat materials. Thus, we searched the parameter space for the maximum of the smaller *CNR*s (equivalent to the minimum of the negative *CNR*):

$$\min_{a_i} -\min(CNR_{TNTvPEN}(a_i), CNR_{TNTvPAD}(a_i)) \quad (8)$$

with a_i denoting the appropriate set of parameters. Once again this was performed numerically by gradient descent.

The optimisation on the dual contrast dataset (*Abs$_L$ and Abs$_H$*, top row) gives a *CNR* of 0.7 for both TNT vs pen and TNT vs pad, which is a gain (0.7 vs 0.4) in the TNT vs pad case but a loss (0.7 vs 3.3) in the TNT vs pen case compared to the single contrast values (Fig. 6). This can be expected, since the algorithm simultaneously maximises the relative distance between all material pairs, which is the only possible approach on the assumption that the target material is unknown. This notwithstanding, when all five contrasts are used, a *CNR* of 3.7 is obtained for both TNT vs pen and TNT vs pad, which is higher than all native *CNR* values (3.7 vs 2.2 for TNT vs pad and 3.7 vs 3.3 for TNT vs pen), when the "best of all five" is selected for the latter. Clearly with some degree of prior information being available (e.g., contrast boundaries for the material of interest obtained through previous calibration), the algorithm performance could be significantly improved.

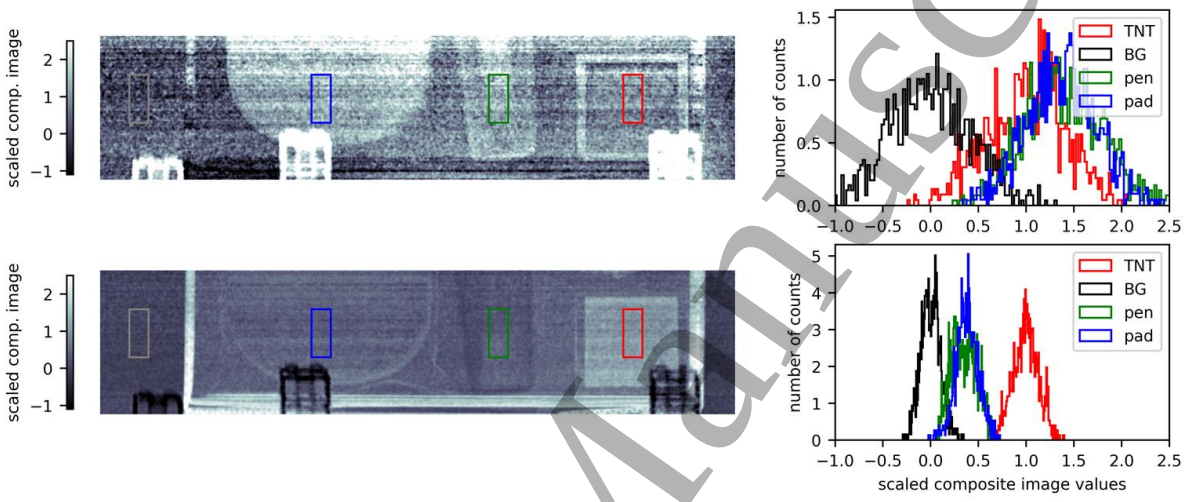

Fig 7 CNR optimisation at a 35 keV threshold for two (Abs$_L$ and Abs$_H$, top row) and five (bottom row) contrasts. The re-scaled composite images are shown on the left. Corresponding histograms extracted from the selected ROIs are shown at the right-hand side of each image, and labelled accordingly (BG = background, i.e., the cardboard box).

Also, in this case results at detector thresholds of 26 and 44 keV are reported for completeness in the supplementary materials (Suppl. Fig. 6 to 9). At 26 keV, optimal *CNR*s of 0.9 and 1.9 are obtained for TNT vs pad and TNT vs pen with two contrasts, versus maximum native values of 0.7 and 2.6. For the five-contrast combination, the *CNR* becomes 2.1 for TNT vs both materials, leading to a gain in the pad case (vs 1.8) but a loss in the pen case (vs 2.6, as reported above). At 44 keV, an optimal *CNR* of 1.6 is obtained for TNT vs both materials with two contrasts, versus maximum native values of 1.2 and 1.5, leading to a small gain in both cases. With five contrasts, however, the gain is more significant with a *CNR* of 4.3 for TNT vs both materials, vs native maxima of 1.6 (TNT-pad) and 3.4 (TNT-pen). This is an even greater gain than observed at 35 keV, which supports the trend observed in Suppl. Fig. 1 in which higher threshold values seem to be slightly more advantageous. While this would seem to support the assumption of a slightly thicker gold layer in the masks, it should also be noted that the simplistic model based purely on noise behaviour we used to obtain fig. 3(b) and Suppl. Fig. 1 may be insufficient to describe the increasingly complex case where multiple materials are present and their respective *CNR*s need to be simultaneously maximised.

		CNR	a_1	a_2	a_3	a_4	a_5
dual-energy	approximative		0.60	0.40			
	phantom 1	8.7	0.80	0.20			
	phantom 2	0.7, 0.7	0.46	0.54			
5 contrasts	approximative		0.24	0.16	0.082	0.48	0.029
	phantom 1	16.3	0.15	0.30	0.50	0.055	0.006
	phantom 2	3.7, 3.7	0.41	0.40	0.024	0.11	0.057

Tab 1: Comparison between dual-energy and 5 contrast results for an energy threshold of 35 keV. The CNR column refers to the experimentally obtained CNR between threat materials (Semtex for phantom 1, TNT for phantom 2) and non-threat materials (paper for phantom 1, pad and pen for phantom 2). The columns labelled a_1-$a_5$refer to the weights in the linear combination of contrasts channels (eq. 2) that optimize the CNR between threat and non-threat materials. The rows labelled 'approximative' refer to the weights as implied by the initial, coarse estimation based on background noise alone (Fig. 3b).

Table 1 summarises the results of theoretical and experimental *CNR* optimisation and provides the determined weights a_1-a_5 used for creating the composite images according to eq. (2). Row entries labelled with 'approximative' refer to the rough estimation based on the background noise (Fig. 3b). Since this was done without the knowledge of specific material contrasts, *CNR* values are not available. The corresponding entries for the weights are simply the inverse relative uncertainties squared as implied by eq. (5) and Fig 3b.

Rows labelled 'phantom 1' (Figs 5 & 6) and 'phantom 2' (Figs 7 & 8) display the retrieved *CNR*s as described above, while also showing alongside the retrieved optimal weights. In the 5 contrast case the main contribution to the composite image for phantom 1 was the *Offset* channel (a_3), i.e., the absorption contrast corresponding to the spectrum filtered by the septa of the masks. For phantom 2 the main contribution arises almost equally from the low and high energy absorption channels Abs_L and Abs_L. The total contribution of the scattering channels was 6% and 17%, which might seem low. However, it should be noted that we have deliberately chosen non-threat materials with strong scattering. This was done in order to provide a challenge for the discrimination of threat vs. non-threat materials using additional scattering contrasts. With this in mind, we can conclude that using 5 instead of 2 contrast channels improves the detection of threat materials.

In Tab 1 it is apparent that the individual weights vary between the different rows. The difference between the rough theoretical estimates (rows labelled 'approximative') and the experimental ones does not come as a surprise, as the former does not take into account the specific contrast of materials. However, the weights vary also between the experimental phantoms, which is due to the different materials used. Here, we want to emphasise that we are demonstrating a potential benefit of utilising 5 instead of 2 contrast channels by a simple analysis of *CNR* gains in the composite images on a phantom by phantom basis. We are not proposing to use the presented weights in practical applications: for this the optimal weights have to be determined over a much larger range of materials, which was the approach taken when dual-energy X-ray imaging was adopted.

In the field of threat detection, the issue of concealment arises naturally. In dual-energy X-ray absorption imaging the issue of overlapping objects is partially addressed by the classification into organic and non-organic materials. Here, sample thickness is accounted for in the projected electron density. For X-ray scattering it has been demonstrated that the squares of the scattering signals from overlapping objects add up [37]. Thus, the sample thickness increases the scattering signal but, due to the energy dependency, it does this differently for the low and high energy scattering signals. This gives the opportunity to take sample thickness into account. Further, overlapping a scattering threat material with a purely absorbing concealment material would increase the noise in the scattering signal, but not hide it. Thus, for an effective concealment, a material would have to match the threat material's dual-energy absorption as well as dual-energy scattering properties at the same time. Therefore, adding dual-energy X-ray scattering contrasts to the already utilized dual-energy absorption contrast would alleviate the issue of threat material concealment.

Conclusions

This paper provides proof-of-concept evidence that the inclusion of additional contrast mechanisms in an imaging system can aid the discrimination between materials with similar attenuation characteristics. The study is admittedly preliminary, and used the optimisation of a simple linear combination of two and five contrast to maximise the *CNR* between material pairs and demonstrate the increased detectability that can be provided by the inclusion of additional contrast channels. While the approach is straightforward when applied to material pairs, the inclusion of additional materials leads to an increased degree of complexity, mostly related to the need to maximise the *CNR* between each material pair when no *a priori* information is available on the target material. However, even such a simple framework is sufficient to prove that room for improvement exists, which we hope will trigger further research in this direction. Further, the inclusion of X-ray scattering contrasts in threat detection has a high potential for reducing the ability of concealing explosives.

Acknowledgments

This work was supported by the EPSRC (Grant EP/T005408/1). Additional support was obtained through the Innovative Research Call in Explosives and Weapons Detection 2016. This is a Cross-Government programme sponsored by a number of Departments and Agencies under the UK Government's CONTEST strategy in partnership with the US Department of Homeland Security, Science and Technology Directorate. AO was supported by the Royal Academy of Engineering under their Chairs in Emerging Technologies scheme.

Declaration of Interest

AA, IGH and DB are, or were at the time the research was carried out, Nikon employees. AO is a named inventor on patents owned by UCL protecting the technology used to obtain the described results. PM has no conflicts of interest to disclose.

References

[1] Macdonald RDR 2001 *Proc. SPIE* **4301** 31

[2] Wells K and Bradley DA 2012 *Appl. Radiat. Isot*. **70** 1729

[3] Lehmann LA, Alvarez RE, Makovski A, Brody WR, Pelc NJ, Riederer SJ and Hall LA 1981 *Med. Phys.* **8** 659
[4] Azevedo S, Martz H, Aufderheide M, Brown W, Champley K, Kallman J, Roberson G, Schneberk D, Seetho I and Smith J 2016 *IEEE Trans. Nucl. Sci.* **63** 341
[5] Naydenov SV and Ryzhikov VD 2003 *Nucl. Instrum. Meth. Phys. Res. A* **505** 556
[6] Naydenov SV, Ryzhikov VD and Smith CF 2004 *Nucl. Instrum. Meth. Phys. Res. B* **215** 552
[7] Snigirev A, Snigireva I, Kohn V, Kuznetsov S and Schelokov I 1995 *Rev. Sci. Instrum.* **66** 5486
[8] Davis TJ, Gao D, Gureyev TE, Stevenson AW and Wilkins SW 1995 *Nature* **373** 595
[9] Wilkins SW, Gureyev TE, Gao D, Pogany A. and Stevenson AW 1996 *Nature* **384** 335
[10] Bonse U and Hart M 1965 *Appl. Phys. Lett.* **6** 155
[11] Rigon L, Besch HJ, Arfelli F, Menk RH, Heitner G and Plothow-Besch H 2003 *J. Phys. D: Appl. Phys.* **36** A107
[12] Pagot E, Cloetens P, Fiedler S, Bravin A, Coan P, Baruchel J, Hartwig J and Thomlinson W 2003 Appl. Phys. Lett. **82** 3421
[13] Oltulu O, Zhong Z, Hasnah H, Wernick MN and Chapman D 2003 *J. Phys. D: Appl. Phys.* **36** 2152
[14] Yashiro W, Terui Y, Kawabata K and Momose A 2010 *Opt. Exp.* **18** 16890
[15] Strobl M 2014 Sci. Rep. **4** 7243
[16] Pfeiffer F, Weitkamp T, Bunk O and David C 2006 *Nat. Phys.* **2** 258
[17] Olivo A and Speller R 2007 *Appl. Phys. Lett.* **91** 074106
[18] Pfeiffer F, Bech M, Bunk O, Kraft P, Eikenberry EF, Brönniman Ch, Grünzweig C and David C 2008 *Nat. Mater.* **7** 134
[19] Endrizzi M, Diemoz PC, Millard TP, Jones JL, Speller RD, Robinson IK and Olivo A 2014 *Appl. Phys. Lett.* **104** 024106
[20] Olivo A, Arfelli F, Cantatore G, Longo R, Menk RH, Pani S, Prest M, Poropat P, Rigon L, Tromba G, Vallazza E and Castelli E 2001 *Med. Phys.* **28** 1610
[21] Olivo A 2021 *J. Phys.: Condens. Matter* **33** 363002
[22] Pacella D 2015 *Rep. Med. Imaging* **8** 1
[23] Astolfo A, Endrizzi M, Vittoria FA, Diemoz PC, Price B, Haig I and Olivo A 2017 *Sci. Rep.* **7** 2187
[24] Buchanan I, Astolfo A, Endrizzi M, Bate D and Olivo A 2022 *Appl. Phys. Lett.* **120** 124102
[25] Sellerer T, Mechlem K, Tang R, Taphorn KA, Pfeiffer F and Herzen J 2021 *IEEE Trans. Med. Imaging* **40** 974
[26] Endrizzi M, Astolfo A, Vittoria FA, Millard TP and Olivo A 2016 *Sci. Rep.* **6** 25466
[27] Astolfo A, Buchanan I, Partridge T, Kallon GK, Hagen CK, Munro PRT, Endrizzi M, Bate D,and Olivo A 2022 *Sci. Rep.* **12** 3354
[28] Poludniowski GG and Evans PM 2007 *Med. Phys.* **34** 2164
[29] Poludniowski GG 2007 *Med. Phys.* **34** 2175
[30] Poludniowski G, Landry G, DeBlois F, Evans PM and Verhaegen F 2009 *Phys. Med. Biol.* **54** N433
[31] Modregger P, Pinzer BR, Thüring T, Rutishauser S, David C and Stampanoni M 2011 *Opt. Exp.* **19** 18324
[32] Munro PRT, Hagen CK, Szafraniec MB and Olivo A 2013 *Opt. Exp.* **21** 11187
[33] Modregger P, Endrizzi M and Olivo A 2018 *Appl. Phys. Lett.* **113** 1–5 254101

[34] James F *Statistical Methods in Experimental Physics* 2006 World Scientific Publishing, 2nd ed.
[35] Buchanan I, Kallon G, Beckenbach T, Schulz J, Endrizzi M and Olivo A 2020 *J. Appl. Phys.* **128** 214503
[36] Zambon P, Radicci V, Trueb P, Disch C, Rissi M, Sakhelashvili T, Schneebeli M and Broennimann C 2018 *Nuclear Inst. and Methods in Physics Research A* **892** 106
[37] Doherty A, Savidis S, Astolfo A, Massimi L, Djurabekova N, Navarrete Leon C, Gerli M, Iacoviello F, Shearing P, Norman D, Williams MA, Olivo A and Endrizzi M 2022 Proc. SPIE Optical Engineering + Applications **12242** 1224209